PROCEEDINGS, Twenty-Eighth Workshop on Geothermal Reservoir Engineering
Stanford University, Stanford, California, January 27-29, 2003
SGP-TR-173

NUMERICAL SIMULATION OF NOBLE GASES AS NATURAL TRACERS FOR INJECTION RETURNS AND RESERVOIR PROCESSES IN VAPOR-DOMINATED SYSTEMS

Chao Shan and Karsten Pruess

Earth Sciences Division, Lawrence Berkeley National Laboratory
University of California
Berkeley, CA 94720, USA
e-mail: k_pruess@lbl.gov

ABSTRACT

Noble gases have attributes and properties that make them very attractive as tracers for fluid movement and reservoir processes. Noble gases are non-reactive and most of them have no sinks or sources in the subsurface, rendering them conservative. They occur naturally in waters that have been in contact with the atmosphere in concentrations that depend on their solubilities. As solubilities are temperature-dependent, noble gas concentrations in subsurface waters may be used to infer the temperature of recharge. Noble gases partition between aqueous and gas (vapor) phases, which alters concentrations in ways that may allow inferences on boiling and condensation processes in two-phase systems. We have developed a fluid property module for TOUGH2 that represents single- and two-phase mixtures of water, noble gases, and air. It includes dependence of solubilities and diffusivities on noble gas species, and on temperature and pressure conditions. This is applied to model transport of noble gases under conditions corresponding to The Geysers vapor-dominated system. Our calculations demonstrate that spatial and temporal variations in noble gas concentrations can be used to track the migration of injected fluids, and to evaluate the extent of vaporization of such fluids. Diffusive exchange between fractures and matrix blocks imparts a characteristic signature on breakthrough curves (BTCs) for noble gases, which may allow inferences on fracture spacing.

INTRODUCTION

An ideal tracer should be non-reactive, non-toxic, and inexpensive. Most noble gases (except radon) satisfy these requirements. In addition, there are usually no sources and sinks for noble gases in the subsurface. As a result, noble gases are usually conservative. The application of noble gases as tracers for subsurface study started many decades ago. Carter et al. (1959) and Gupta et al. (1994) used helium for groundwater studies. Divine (2000) used helium and neon as partitioning tracers to characterize dense non-aqueous phase liquids (DNAPLs). Pruess et al. (2000) performed numerical simulation studies to evaluate the use of neon and xenon as tracers to characterize geothermal reservoir processes. The application of noble gases can also be found in other studies (e.g., Sugisaki, 1961; Sanford et al., 1996; Sanford and Solomon, 1998).

In this study, we evaluate the feasibility of using noble gases to characterize a fractured geothermal reservoir. We will focus on estimation of fracture spacing based on predetermined matrix hydraulic properties. The tool used for such a study is TOUGH2/EOSN, a new fluid property module for noble gas transport.

MODEL DESCRIPTION

Starting from TOUGH2/EOS7R, we have developed a fluid property module EOSN that can be applied to two-phase, five-component flow and transport problems. The two phases are aqueous and gas, and the five components are water, brine, air and two user-selected noble gases. The program simulates important transport processes such as advection, adsorption, phase change (evaporation and condensation), phase partitioning, and gas diffusion. The phase partitioning is simulated using Henry's law. According to Henry's law, the partial pressure of a non-condensable gas (*NCG*) in the gas phase is proportional to the mol fraction (x) of the dissolved *NCG* in the aqueous (aq) phase (Prausnitz et al., 1986):

$$P_{NCG} = K_h x_{aq}^{NCG} \tag{1}$$

Gas diffusion is calculated using Fick's law. According to Fick's law, the diffusive flux of component κ in phase β (= aqueous, gas) is given by

(Pruess et al., 1999)

$$\mathbf{f}_{\beta}^{\kappa} = -\phi\tau_0\tau_{\beta}\rho_{\beta}d_{\beta}^{\kappa}\nabla X_{\beta}^{\kappa} \qquad (2)$$

where ϕ is porosity, $\tau_0\tau_\beta$ is the tortuosity that includes a porous medium dependent factor τ_0 and a coefficient τ_β that depends on phase saturation S_β, $\tau_\beta = \tau_\beta\ (S_\beta)$, ρ_β is density, d_β^κ is the diffusion coefficient of component κ in bulk fluid phase β, and X_β^κ is the mass fraction of component κ in phase β.

Each law is characterized by a coefficient: the Henry's law coefficient and the diffusion coefficient, which are both temperature/pressure dependent. At every time step and iteration, TOUGH2/EOSN substitutes the most up-to-date temperature/pressure to two models for updating the two coefficients. It uses the theoretical model given by Reid et al. (1987) to calculate the noble gas diffusivity in the gas phase, and the laboratory experiment-based Crovetto et al. (1982) model to calculate the Henry's law coefficient. Figures 1A and 1B show the temperature-dependent gas phase diffusivities and Henry's law coefficients for air and six gases calculated by the above models. Note that Figure 1A depicts diffusivity at saturation pressure corresponding to temperature. The reason for diffusivities going to such large values at low temperatures is their inverse dependence on pressure.

APPLICATION TO FIVE-SPOT PRODUCTION-INJECTION PROBLEM

The problem was designed according to conditions in The Geysers reservoir (Pruess et al., 2000). To simplify the numerical simulation we take advantage of problem symmetries by assuming that production and injection wells are arranged in a regular five-spot pattern (see Figure 2). A single layer of 500 m thickness is modeled, and a five-point parallel grid of 196 square blocks with 10.88 m length is used to represent a 1/8 symmetry element. Numerical simulations were conducted for two saturation cases, three injection schedules, and four reservoir-geology scenarios. Thus, there were 24 simulations. The initial water saturation in matrix block or porous medium is 0.068 in Case 1 (the depleted case), and 0.99 in Case 2 (the undepleted case). The initial water saturation in the fractures is the same (0.0001) for both cases. The overall production and injection rates are 8 kg/s (full well basis) for both cases. Field observations at The Geysers have shown that under depleted conditions, injected water is rapidly and completely vaporized near the injection well (Beall et al., 1994, 1998). Accordingly, to simplify the numerical simulation problem, we directly apply

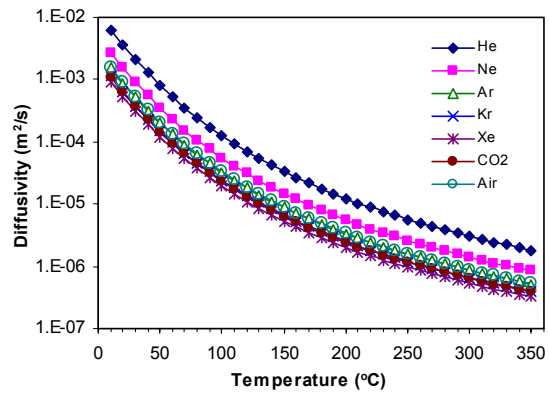

Fig. 1A. Diffusivity for air and six gases in saturated water vapor as a function of temperature.

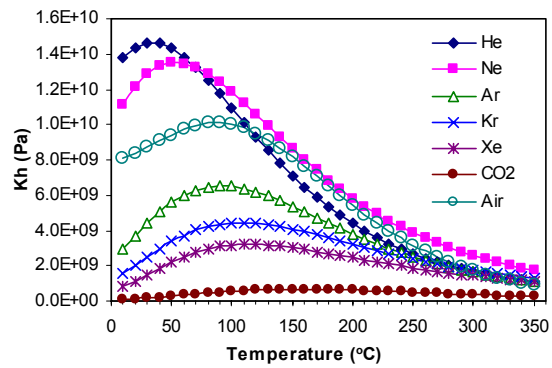

Fig. 1B. Henry's law coefficient as a function of temperature for air and six gases.

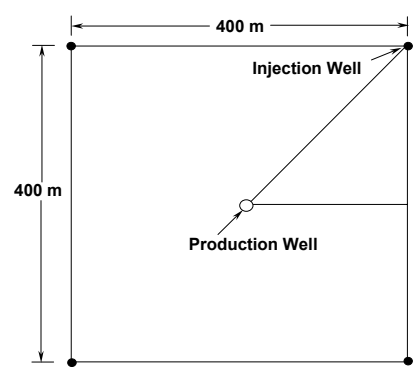

Fig. 2. Five-spot well pattern, with the triangular area showing a 1/8-symmetry element.

injected fluid as vapor in this case (injection enthalpy 2800 kJ/kg). In Case 2 (the undepleted case), we injected water by specifying an injection enthalpy of 125 kJ/kg (corresponding to water at temperature of 29.8°C). Three schedules were designed for noble gas injection. Schedule 1 assumed a steady injection of noble gases with a concentration of 0.0488 ppb for Ne, and 0.0428 ppb for Xe. These concentrations

represent the ones that can be found in waters in contact with the atmosphere. Schedules 2 and 3 both assumed an 8-hour noble gas injection with a concentration of 1 ppm for both Ne and Xe (the corresponding partial pressures are P_{ne} = 12.9 Pa and P_{xe} = 1.5 Pa at 29.8°C; P_{ne} = 4.2 Pa and P_{xe} = 2.0 Pa at 240°C). The slug injection started at the beginning for schedule 2 (t_0 = 0), and at t_0 = 30 days for schedule 3. The first three reservoir-geology scenarios are fractured reservoir with an average fracture spacing (FS) of 10 m, 20 m, and 50 m, respectively. For purpose of comparison, a reservoir composed of uniform porous medium (UPM) was simulated as the fourth scenario. The fractured porous medium is modeled using the method of multiple interacting continua ("MINC;" Pruess and Narasimhan, 1985). More detailed problem specifications as given in Table 1 are similar to what was used in previous work (Pruess et al., 2000; Pruess, 2002)

Table 1. Specifications of Five-spot Problem

Reservoir properties	
Permeability (fracture & porous medium)	43.2×10^{-15} m^2
Permeability (matrix)	1.9×10^{-18} m^2
Porosity (fracture)	1%
Porosity (matrix)	3%
Porosity (porous medium)	4%
Thickness	500 m
Fracture spacing	10 m, 25 m, 50 m (Scenario 1, 2, 3)
Relative permeability aqueous: van Genuchten (1980); parameters gas: Corey (1954); parameter	m = .4438 S_{gr} = .05 S_{lr} = .08 (fracture & matrix)
Capillary pressure van Genuchten (1980); parameters	m = .4438; S_{lr} = 0; P_0 = 3238 Pa (fractures); 1.727×10^6 Pa (matrix)
Pattern area	160,000 m^2 (= 39.5 acres)
Well spacing (distance from injector to producer)	282.8 m (928.0 ft)
Production/injection rate (full well basis)	8 kg/s
Injection enthalpy	2800 kJ/kg (Case 1); 125 kJ/kg (Case 2)
Gridding	
5-point parallel grid, spacing	10.88 m
Initial conditions	
Pressure	33.479 bar
Temperature	240°C
Water saturation in fractures in matrix	0.0001 0.068 (Case 1); 0.99 (Case 2)
Tracer injection	
Ne	Steady injection: 0.0488 ppb Slug injection: 8 hours at 1 ppm
Xe	Steady injection: 0.0428 ppb Slug injection: 8 hours at 1 ppm

RESULTS

The calculated mass fractions of Ne and Xe in the gas phase at the production well are presented in terms of breakthrough curves (BTCs) for Ne and curves for Xe/Ne mass fraction ratios. In all simulations of a fractured reservoir, the injection and production wells are placed in the fracture elements at corresponding locations. The BTCs are plotted on a linear scale as well as a semi-log scale to obtain a clear view of the tail-section. The results for the three schedules in Case 1 are shown in Figure sets 3, 4, and 5, respectively. The results for the three schedules in Case 2 are shown in Figure sets 6, 7, and 8, respectively. Most sets contain three figures: A is a BTC plot on a linear scale, B is the BTC plot on a semi-log scale, and C is a plot of Xe/Ne mass fraction ratio.

There are several important points for analyzing the results: 1) the transport of noble gases is mainly through advection and diffusion in the gas phase, especially in a depleted reservoir; 2) condensation increases water saturation, decreases the cross-sectional area of the gas channel and thus reduces noble gas transport; and 3) evaporation, on the contrary, helps open and enlarge gas channels and thus enhances noble gas transport.

Figure 3A shows the BTCs for mass fraction of Ne under injection schedule 1 (constant noble gas concentration) and for Case 1 (depleted conditions). It is not surprising that all curves rise rapidly at the beginning, when fractures are largely open for gas phase transport. The figure also shows that the mass fraction increases faster for larger fracture spacing (e.g., FS = 50 m) because of less sink effect from the matrix blocks. This feature can be useful in estimating the average fracture spacing for a reservoir (see below). At intermediate time, all BTCs for the fractured reservoir demonstrate certain fluctuations. Although a coarse grid usually causes numerical fluctuations, there are different causes for this case. A study on detailed output information reveals that two major mechanisms behind this phenomenon are the condensation-evaporation effect and the fracture-matrix interaction. The injection-production process caused pressure and temperature changes and thus initiated a condensation process starting from the injection well where water vapor was injected. Although the fractures were initially available for the gas phase transport, the condensation in fractures reduced the space for gas. Since both advection and diffusion are strongly affected by the cross-sectional area, as condensation went on the transport of noble gases towards the production well slowed down. In fact, the increase of noble gas mass fractions at the production well decreased the concentration gradient and thus also had an impact on reduction of diffusive fluxes. This was a gradual process, and when it reached a point (e.g., t = 155 days for FS = 10 m in Figure 3A) the mass fraction stopped going up and started coming down. The condensation might continue at areas close to the injection well at this time. Other areas close to the production well, however, speeded up evaporation to provide mass supply to the production well. The decrease of mass fraction continued for a while because of less supply of noble gas from the injection well and more supply of water vapor evaporated from the surrounding area of the production well. During this period of time, the matrix blocks close to the injection well absorbed more injected noble gases as well as water vapor. When the system reached a non-sustainable point (e.g., t = 195 days for FS = 10 m in Figure 3A), at the injection well area condensation stopped and evaporation started, which opened the space for the gas phase transport. In this period, the stored noble gases in the matrix block diffused back to the fracture channels, causing the mass fraction at the production well to go up. The fluctuations continue for a few cycles and finally stabilize at a constant value, the injection concentration. For the uniform porous medium, the condensation front simply initiated around the injection well, then moved toward the production well, and thus only causes minor fluctuations (Figure 3A). We do not present the BTCs for Xe because their shapes look similar. Instead, we compare two noble gases by looking at the Xe/Ne mass fraction ratio (Figure 3B). For all four scenarios, the ratio approaches a value close to the injected mass fraction ratio (0.88). At early time, however, there is a relatively large increase of the ratio for smaller fracture spacing (FS = 10 m and 25 m). Small fracture spacing offers large interfacial area between fractures and matrix blocks. At early time and in a depleted reservoir, gas diffusion is a major transport process into the matrix blocks. At 240°C, the diffusivity of neon is almost three times larger than that of xenon (Figure 1A), and the Henry's law coefficient for neon is twice that for xenon (Figure 1B). This means that more neon is in the gas phase, and that more neon diffuses into the matrix. As a result, less neon can reach the production well. This situation changes later as matrix-stored neon diffuses back into the fractures. The early time increase of mass fraction ratio can be useful in characterizing fracture spacing.

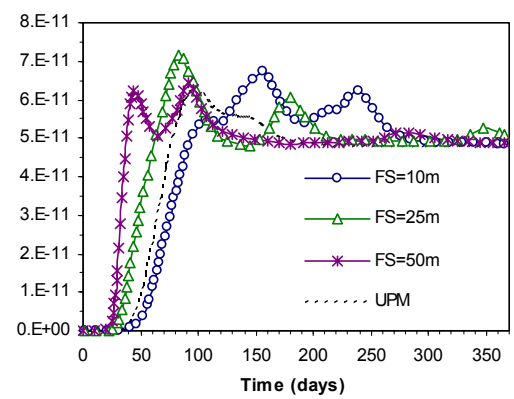

Fig. 3A. Breakthrough curves for neon under steady injection in depleted reservoir.

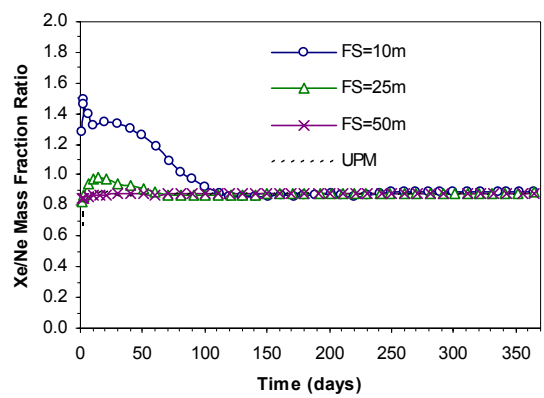

Fig. 3B. Xe/Ne mass fraction ratio under steady injection in depleted reservoir.

For an 8-hour slug injection of noble gas, Figures 4A through 4C show the results for schedule 2 where the injection of noble gases started at t_0 = 0. Like most other tracer test results, there are bell-shaped BTCs in Figure 4A (a linear scale plot) for all scenarios. For larger fracture spacing, the peak of the BTC

increases, while the width of the BTC decreases. The peak of the BTC occurs at earlier time for larger fracture spacing. The peak and location of the BTC on a linear scale plot are useful for fracture spacing estimation, while the tail of the BTC on a semi-log plot (Figure 4B) may serve the same purpose. Small fracture spacing significantly increases the fracture-matrix interfacial area, thus more noble gases is stored in the matrix at earlier time and released at later time, producing stronger tails. On Figure 4C, we see a similar early time pattern as that on Figure 3B. We also see that the storage effect of matrix blocks causes the neon mass fraction to be much greater than that of xenon at later times. In a slug test, the stored tracer in the matrix plays a major role after the tracer injection is shut off. On Figure 4C, the mass fraction ratio for the uniform porous medium scenario always remains close to the injection ratio (1.0). Consequently, it is the fracture-matrix interaction that causes the deviation.

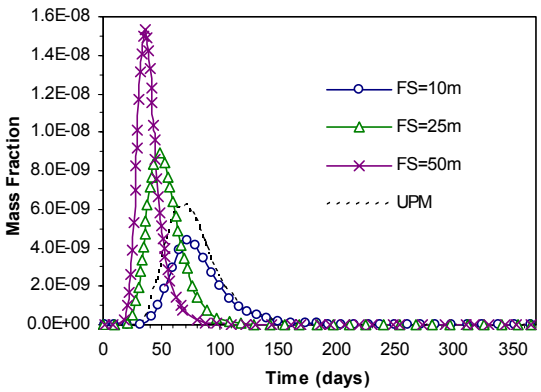

Fig. 4A. Breakthrough curves for neon under 8-hour slug injection ($t_0 = 0$) in depleted reservoir.

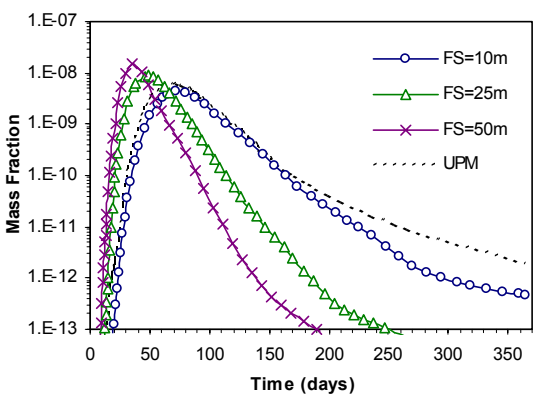

Fig. 4B. Breakthrough curves for neon under 8-hour slug injection ($t_0 = 0$) in depleted reservoir.

The results for an 8-hour slug injection started after 30 days of operation (schedule 3) in Case 1 are shown in Figures 5A through 5C. The BTCs look similar to the corresponding ones in Figures 4A and 4B. A close look at these figures reveals that some differences do exist. Compared with Figure 4A, the

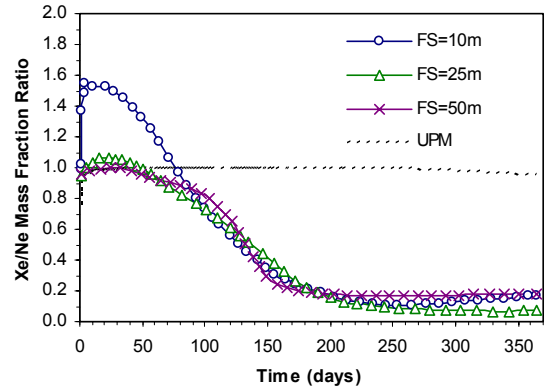

Fig. 4C. Xe/Ne mass fraction ratio under 8-hour slug injection ($t_0 = 0$) in depleted reservoir.

BTCs in Figures 5A and 5B reach their peaks faster after slug injection at $t = 30$ days. The BTC peaks are higher in Figures 5A and 5B. This is because after 30 days of injection, there is a quasi-steady pressure field close to the injection well, and less tracer is pushed into the matrix blocks. As a result, more noble gases could reach the production well more rapidly. Taking FS = 50 m as the scenario for comparison, the time to reach the BTC peak is about 36 days for schedule 2 and 21.5 days for schedule 3.

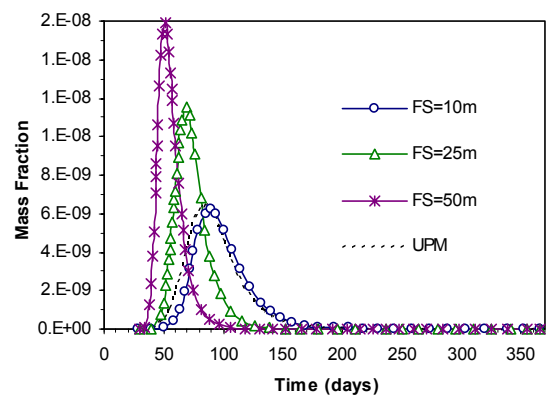

Fig. 5A. Breakthrough curves for neon under 8-hour slug injection ($t_0 = 30$ days) in depleted reservoir.

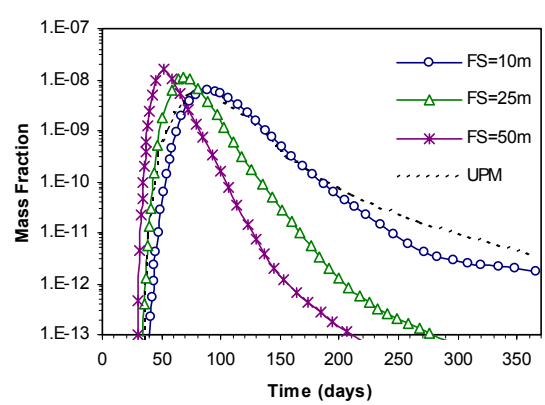

Fig. 5B. Breakthrough curves for neon under 8-hour slug injection ($t_0 = 30$ days) in depleted reservoir.

Since the storage effect for neon is less than that of the previous schedule (schedule 2), the mass fraction ratio for FS = 10 m demonstrates a later rise (still less than one) as shown in Figure 5C. It should be noted that in a slug injection test, when the noble gas mass fractions (or concentrations) are very low at later time, the calculated ratio becomes less reliable.

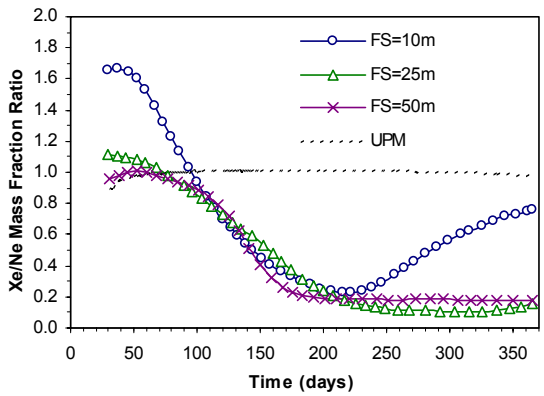

Fig. 5C. Xe/Ne mass fraction ratio under 8-hour slug injection (t_0 = 30 days) in depleted reservoir.

In Case 2, the matrix was initially saturated with water (0.99 of water saturation), leaving little room for gas. The injected water is in liquid phase. For the scenario of a uniform porous medium, the transport is mainly dependent on dissolved noble gases in moving water. All results for the porous medium scenario showed no meaningful detections at the production well in the period of simulation (1 year). Therefore these results are only shown on the BTC plots on a linear scale (Figures 6A, 7A, and 8A). For the three fracture scenarios, however, advection and diffusion of noble gas through fractures were weaker but still significant.

For a continuous injection, the BTCs shown in Figure 6A break much later and rise much slower than those in Figure 3A. Being buffered by water, the BTCs are also much smoother. Only the curve for FS = 10 m showed minor fluctuations (Figure 6A). Similar to the counterpart in Figure 3A, the mass fraction curves break earlier for larger fracture spacing. In this case, soon after the start of injection, the initially gas-saturated fractures became water saturated. Then the production well started dewatering its surrounding area, and the injected water with tracer started filling the matrix blocks as well as fractures and moving forward. The matrix storage effect still exists but is weaker and delayed (Figure 6B).

The slug injections of noble gases in Case 2 give similar results as the corresponding ones of Case 1. Figures 7A and 8A show the BTCs for 8-hour slug injection at t_0 = 0, and 30 days, respectively. Both figures show an earlier breakthrough for larger fracture spacing. Compared with the corresponding

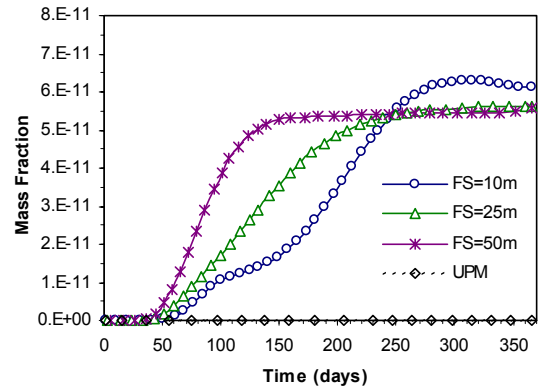

Fig. 6A. Breakthrough curves for neon under steady injection in undepleted reservoir.

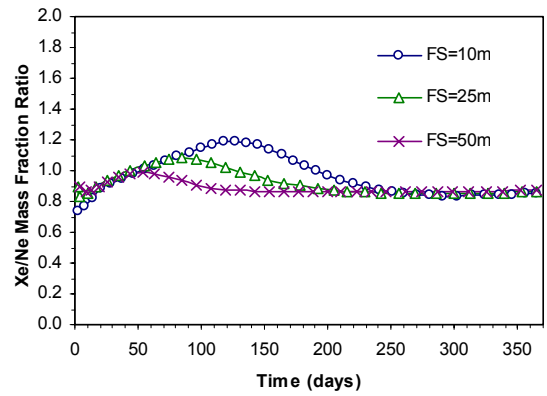

Fig. 6B. Xe/Ne mass fraction ratio under steady injection in undepleted reservoir.

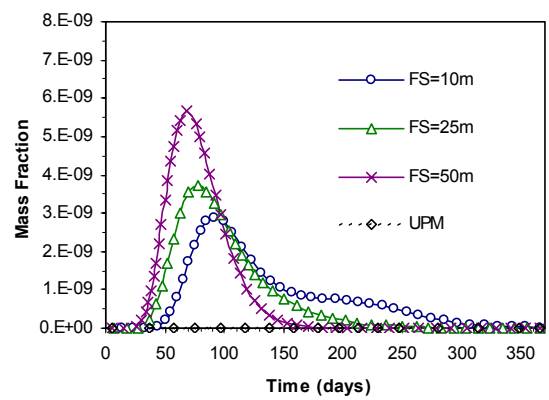

Fig. 7A. Breakthrough curves for neon under 8-hour slug injection (t_0 = 0) in undepleted reservoir.

counterparts in Case 1, the breakthroughs are generally much delayed, and the peaks of the curves are generally much weaker. The comparison between Figures 7A and 8A also shows some differences. The shape of the two BTCs for FS = 50 m are almost the same, but the BTC in Figure 8A (slug injection for noble gases after 30 days) is delayed for about 30 days. The shapes of BTCs corresponding to FS = 10 m (and 25 m), however, are different in Figures 7A and 8A. This is probably due to a slower fracture

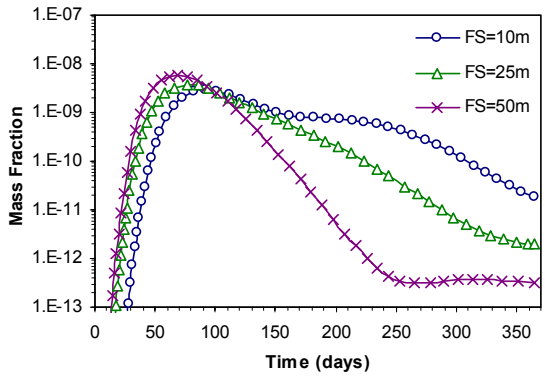

Fig. 7B. Breakthrough curves for neon under 8-hour slug injection (t_0 = 0) in undepleted reservoir.

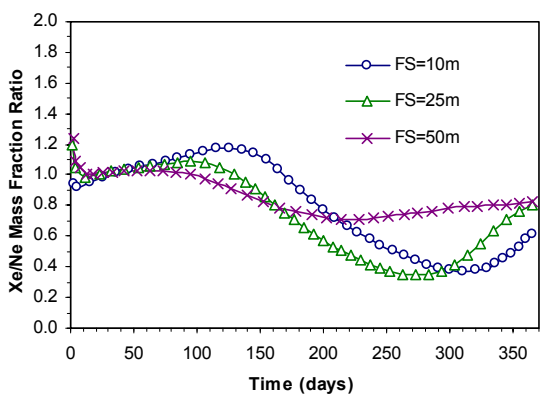

Fig. 7C. Xe/Ne mass fraction ratio under 8-hour slug injection (t_0 = 0) in undepleted reservoir.

dewatering for smaller fracture spacing. While the 30 days of delay in injection does not cause noticeable difference for the scenario of FS = 50 m, it does have relatively large impact for the other two scenarios of FS = 10 m and 20 m. The delay of noble gas injection conserves more injected noble gases for a slow but longer release. Figures 7B and 8B show different tails of the BTCs on the semi-log plots. The Xe/Ne mass fraction ratios from the two slug injection simulations for Case 2 show some delayed and weaker matrix storage effects (Figures 7C and 8C). All of them, however, have distinguishable differences among different scenarios, which can be useful in fracture spacing estimation.

In the above studies we used a fixed injection-production rate (8 kg/s). Further studies have shown that this rate has an impact on the arrival time of BTC peak as well as the peak magnitude. For example, for the scenario of FS = 50 m, the arrival time is about 36 days for a rate of 8 kg/s, 23 days for a rate of 12 kg/s, and 10 days for a rate of 16 kg/s (Pruess, 2002; using R-134a and tritium). The rate, however, will be limited by practical reservoir conditions.

Based on numerical simulations on slug tests, we can prepare useful tools for estimating average fracture

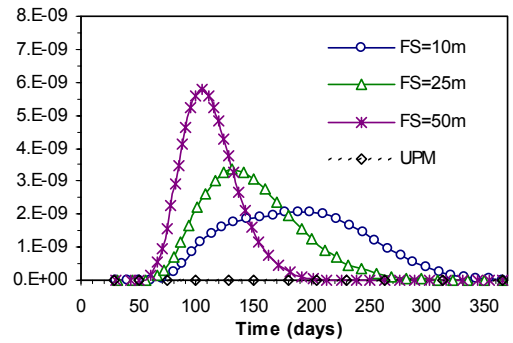

Fig. 8A. Breakthrough curves for neon under 8-hour slug injection (t_0 = 30 days) in undepleted reservoir.

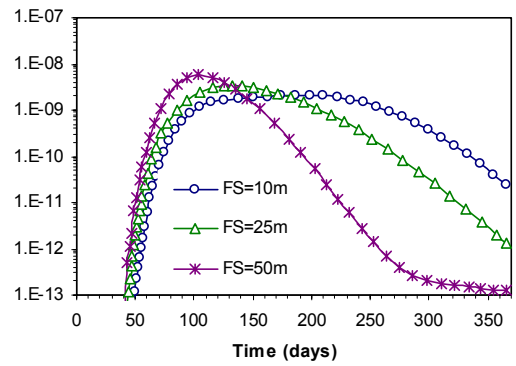

Fig. 8B. Breakthrough curves for neon under 8-hour slug injection (t_0 = 30 days) in undepleted reservoir.

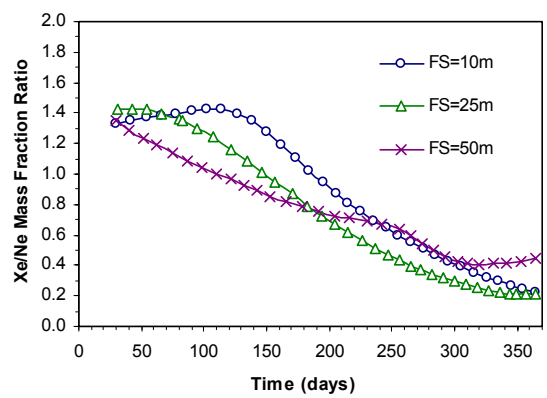

Fig. 8C. Xe/Ne mass fraction ratio under 8-hour slug injection (t_0 = 30 days) in undepleted reservoir.

spacing. For example, we can plot the following characteristic parameters as a function of fracture spacing (FS): x_P (relative peak value, the ratio of the peak and injected concentrations), t_P (peak time), and t_D (decay time, when concentration decreases to 1/10 of the peak value). Using the data from Figure 4A (an early slug injection for Case 1), we prepared the three plots in Figure 9, which shows that the breakthrough is more rapid and occurs with higher concentrations for larger fracture spacing. Observed field parameters (x_P, t_P, or t_D) can be used to check out the average fracture spacing by means of prepared plots like those in Figure 9.

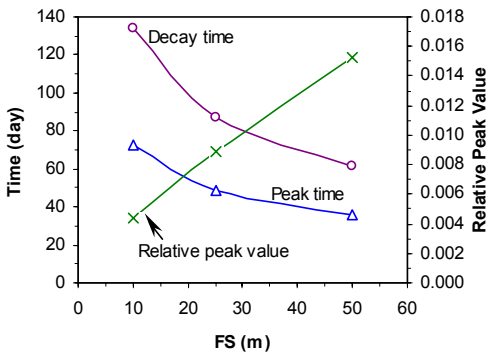

Fig. 9. Relative peak value, peak time, and decay time as a function of average fracture spacing; for Ne 8-hour slug injection ($t_0 = 0$) in depleted reservoir.

CONCLUSIONS

TOUGH2/EOSN is a useful tool for simulating noble gas transport in the subsurface. The applications to the five-spot injection-production problem have demonstrated sensitivity of breakthrough curves to average fracture spacing. When using noble gases as tracers, both continuous and slug injections can provide breakthrough curves that are useful for the estimate of fracture spacing. Large fracture spacing results in earlier breakthrough and reduced tailing due to reduced fracture-matrix interaction. When two noble gases such as neon and xenon are used, the mass fraction ratio of the two noble gases provides some additional information for estimating average fracture spacing. The tracer tests can be conducted in either a depleted or an undepleted reservoir.

ACKNOWLEDGEMENT

This work was supported by the Assistant Secretary for Energy Efficiency and Renewable Energy, Office of Geothermal Technologies, of the U.S. Department of Energy under contract No. DE-AC03-76SF00098. We thank Stefan Finsterle and Tianfu Xu for reviewing the manuscript.

REFERENCES

Beall, J. J., M. C. Adams, and P. N. Hirtz, (1994), R-13 tracing of injection in The Geysers, *Transactions Geothermal Resources Council* 18: 151-159.

Beall, J. J., M. C. Adams, and P. N. Hirtz, (1998), Evaluation of R-134a as an injection water tracer in the Southeast Geysers, *Transactions Geothermal Resources Council* 22: 569-573.

Carter, R. C., W. J. Kaufman, G. T. Orlob, and D. K. Tood, (1959), Helium as a groundwater tracer, *J. Geophys. Res.* 64: 2433-2439.

Corey, A. T., (1954), The interrelation between gas and oil relative permeabilities, *Producers Monthly,* pp. 38-41.

Crovetto, R., R. Fernandez-Prini, and M. L. Japas, (1982), Solubilities of inert gases and methane in H2O and in D2O in the temperature range of 300 to 600 K, *J. Chem. Phys*. 76(2): 1077-1086.

Divine, C. E., (2000), The applicability of dissolved helium and neon as dense nonaqueous phase liquids (DNAPL) partitioning tracers, *M. S. Thesis,* Colorado State University, Fort Collins, Colorado.

Gupta, S. K., P. S. Moravcik, and L. S. Lau, (1994), Use of injected helium as a hydrological tracer, *Hydrological. Sci. J.,* 39: 109-119.

Prausnitz, J. M., R. N. Lichtenthaler, and E. G. de Azevedo, (1986), *Molecular Thermodynamics of Fluid-Phase Equilibria*, Prentice-Hall Inc., Englewood Cliffs, N. J.

Pruess, K., (2002), Numerical simulation of multiphase tracer transport in fractured geothermal reservoirs, *Geothermics*, 31: 475-499.

Pruess, K., and T. N. Narasimhan, (1985), A practical method for modeling fluid and heat flow in fractured porous media, *Soc. Pet. Eng. J.*, 25(1): 14-26.

Pruess, K., C. Oldenburg, and G. Moridis, (1999), *TOUGH2 User's Guide*, Version 2.0, Lawrence Berkeley National Laboratory Report LBNL-43134, Berkeley, CA.

Pruess, K., M. J. O'Sullivan, and B. M. Kennedy, (2000), Modeling of phase-partitioning tracers in fractured reservoirs, *Proceedings, Twenty-Fifth Workshop on Geothermal Reservoir Engineering*, Stanford University, Stanford, California, January 24-26, 2000. SGP-TR-165, LBNL-44802.

Reid, R. C., J. M. Prausnitz, and B. E. Poling, (1987), *The Properties of Gases and Liquids*, McGraw-Hill, New York.

Sanford, W. E., R. G. Shropshire, and D. K. Solomon, (1996), Dissolved gas tracers in groundwater: simplified injection, sampling and analysis, *Water Resour. Res*. 32: 1635-1642.

Sanford, W. E. and D. K. Solomon, (1998), Site characterization and containment assessment with dissolved gases, *J. Env. Eng*. 124: 572-574.

Sugisaki, R., (1961), Measurement of effective flow velocity of ground water by means of dissolved gases, *Am. J. of Sci.* 259: 144-153.

van Genuchten, M. Th., (1980), A closed-form equation for predicting the hydraulic conductivity of unsaturated soils, *Soil Sci. Soc. Am. J.,* 44: 892-898.